Contents lists available at ScienceDirect

Applied Catalysis B: Environmental

Optimizing cathode materials for intermediate-temperature solid oxide fuel cells (SOFCs): Oxygen reduction on nanostructured lanthanum nickelate oxides

Juliana Silva Alves Carneiro, Roger Antunes Brocca, Max Laylson Ribeiro Sampaio Lucena, Eranda Nikolla*

Department of Chemical Engineering and Materials Science, Wayne State University, Detroit, MI 48202, USA

ABSTRACT

Kinetics of high temperature oxygen reduction reaction (ORR) on $La_2NiO_{4+\delta}$ (LNO) nanostructures are investigated by means of electrochemical impedance spectroscopy, with the aim of determining (i) the critical steps that govern ORR in these catalysts, and (ii) ways to lower the overpotential losses associated with these steps. We have identified two main electrochemical processes that govern the polarization resistances during ORR: the electron transfer/oxygen vacancy healing ($O_{ads} + 2e^- + \boldsymbol{V_O^{..}} \Leftrightarrow \boldsymbol{O_{O(LNO)}^X}$), and the oxygen ion transfer through the electrocatalyst/electrolyte interface ($\boldsymbol{O_{O(LNO)}^X} + \boldsymbol{V_O^{..}} \Leftrightarrow O_{O(YSZ)}^X$). We find that the nanostructure of LNO significantly effects the activation barriers associated with these processes with nanorod–structured LNO catalyst, highly terminated by [001] surface facets, exhibiting lower barriers compared to traditional, spherical-shaped catalysts. We also show that incorporation of the nanorod–structured LNO as cathode electrocatalysts in SOFCs leads to a significant improvement in the cell performance. These findings provide important insights on the electrochemical steps that govern ORR kinetics on LNO electrocatalyst, and ways to optimize these materials as cathode electrocatalysts for intermediate temperature SOFCs (IT-SOFCs).

© 2016 Elsevier B.V. All rights reserved.

1. Introduction

Oxygen reduction reaction (ORR) plays an important role in many electrochemical energy conversion systems, including solid oxide fuel cells (SOFCs). SOFCs are solid-state electrochemical devices that convert the chemical energy of combustible fuels into electrical energy at elevated temperatures. In these systems, ORR occurs at the cathode and involves the electrochemical reduction of gas phase oxygen to oxygen ions in the presence of electrons ($1/2O_2 + 2e^- => O^{2-}$). This reaction is commonly catalyzed by perovskite-type electrocatalysts that suffer from high overpotential losses, especially when operating under intermediate temperature conditions (500–700 °C) [1]. Recent reports have shown that nickelate oxide electrocatalysts with a layered crystal structure exhibit promising activity for ORR, making these systems promising candidates for intermediate-temperature SOFC cathode materials [2–5].

Nickelate oxides are mixed ionic/electronic conducting (MIEC) materials that belong to first-order Ruddlesden-Popper series, composed of alternating rocksalt and perovskite layers, generally expressed with the formula $A_2MO_{4+\delta}$ [6,7]. They are characterized by the oxygen hyper-stoichiometry in their lattice that is accommodated *via* the rocksalt-like layers [5,8]. It has been reported that lanthanum nickelates ($La_2NiO_{4+\delta}$, LNO) exhibit higher electrochemical ORR activity and improved thermal compatibility with commonly used electrolytes when compared to most traditional perovskite oxides [9]. Furthermore, through a combined theoretical/experimental study, it has been established that the surface structure, controlled by the nanostructure, of lanthanum nickelates plays an important role in their catalytic activity [10,11].

Control over the nanostructure of nickelate oxides can be very challenging when they are incorporated in SOFCs using current state-of-the-art fabrication methods, since these methods involve co-sintering of the electrode electrocatalyst with the electrolyte oxide (*i.e.*, YSZ) at high temperatures (above 1000 °C), leading to chemical instability of the electrocatalyst and formation of undesired oxide phases that act as insulators at the electrode/electrolyte interface [7,19,20]. This can be circumvented by synthesizing

---

* Corresponding author at: 5050 Anthony Wayne Drive, Detroit, MI, 48202, USA.
E-mail address: erandan@wayne.edu (E. Nikolla).

porous scaffolds of ion-conducting oxides, *i.e.* YSZ, at the electrode that can serve as support for the electrocatalytic particles. Porous oxide scaffold SOFC electrodes have been successfully implemented along with infiltration of metal salts for *in-situ* synthesis of oxide electrocatalysts [21–23]. The main challenge with co-infiltration of metal salts on porous scaffolds for *in-situ* synthesis of complex metal oxide electrocatalysts is the limited control over the electrocatalyst nanostructure, and the uniformity in the desired oxide phase within the scaffold matrix. Therefore pre-synthesis of nanostructured oxide electrocatalyst that allows for control over their chemical and geometrical structure is necessary.

In this contribution, we discuss in detail the kinetics of ORR on nanostructured LNO electrocatalyst with the aim of determining (i) the critical steps that govern ORR in these catalysts, and (ii) ways to lower the overpotential losses associated with these steps. Kinetic studies are conducted using symmetric solid oxide electrochemical cells. The LNO nanostructures are synthesized using a reverse microemulsion synthesis method. In order to preserve the nanostructure of the electrocatalyst during the fabrication of the symmetric cells, scaffold-type electrode systems are developed. Our experiments show that the dominant resistances during oxygen reduction on nanostructured LNO electrocatalysts are associated with the vacancy healing/charge transfer step at the electrocatalyst/gas interface and oxygen ion transfer from the electrocatalyst to the electrolyte. We show that the nanostructure of the electrocatalytic particles significantly impacts the energetics associated with these steps, with nanorod-shaped lanthanum nickelate exhibiting the lowest barriers as compared to traditional spherical particles. The apparent activation barriers for these processes on nanorod-shaped LNO are 98.43 ± 0.87 kJ/mol and 103.08 ± 2.78 kJ/mol, respectively. The overall barrier obtained for ORR on LNO nanorods is 100.91 ± 1.05 kJ/mol, which is significantly lower than the ones reported for traditional perovskite-type electrocatalysts [12–14]. In agreement with our kinetic data, SOFCs composed of nanorod-shaped LNO cathode electrocatalyst exhibited improved electrochemical performance (higher power density) when compared to the ones composed of LNO nanospheres. These studies lay the groundwork for tuning the electrocatalytic ORR activity of LNO nanostructures, and open up opportunities for utilizing these materials as cathode electrocatalysts for intermediate temperature SOFCs (IT-SOFCs).

2. Experimental methods

2.1. Synthesis of $La_2NiO_{4+\delta}$ nanostructures

All chemicals are used as commercially received without further purification. The nanostructured LNO catalyst is prepared using a reverse-microemulsion assisted sol-gel method, as previously reported [10,11]. Two systems are separately prepared, each one containing a reverse-microemulsion consisting of cetyltrimethylammonium bromide (CTAB)/water/hexane/n-Butanol. The first microemulsion is obtained by mixing $La(NO_3)_3 \cdot 6H_2O$ (99.999%, Sigma Aldrich) and $Ni(NO_3)_2 \cdot H_2O$ (98%, Alpha Aesar) with deionized water. The second one is obtained by mixing NaOH (ACS grade, Fisher) and deionized water. After homogeneity is achieved in both systems, the microemulsion containing NaOH is added to the system containing the metal salts. This final solution is maintained under stirring for 4 h until a gel suspension is obtained. The product is then centrifuged and washed using ethanol and deionized water. This is followed by drying at 80 °C for 12 h and calcination at 825 °C for 2 h under argon.

2.2. Synthesis of electrochemical cells

2.2.1. Symmetric electrochemical cells

Two-electrode, symmetric solid oxide electrochemical cells have been widely used to determine the high temperature ORR kinetics on mixed ionic/electronic conducting oxide electrocatalysts [13,15,24]. These electrochemical systems are characterized by two identical symmetric electrodes that are separated by an oxygen ion-conducting electrolyte, *i.e.*, YSZ. The YSZ membrane is fabricated by dry-pressing sieved (125 μm) YSZ powder (TZ-8Y, Tosoh) followed by sintering at 1450 °C for 4 h in air. Subsequently, a porous YSZ scaffold is synthesized using a ball-milled mixture of YSZ (70 wt%), graphite (30 wt%, 99.9995%, 325 mesh, Alpha Aesar), fish oil (Sigma, from Menhaden), butyl benzyl phthalate (Richard E. Mistler Inc.), polyalkylene glycol (The Dow Chemical Company), and polyvinyl butyral (Richard E. Mistler Inc.), which is sprayed symmetrically on both sides of the sintered YSZ membrane. The assembly is heated to 600 °C and then sintered at 1450 °C for 4 h. The LNO nanorods are dispersed in ethanol by sonication, followed by drop coating – ~1 mg of electrocatalyst – over the YSZ scaffold, and curing at 400 °C for 3 h.

2.2.2. Anode-supported SOFCs

Anode-supported SOFCs are synthesized by initially ball-milling NiO (99%, Alpha Aesar), YSZ and graphite (1:1:0.6 wt ratio) in ethanol for 48 h. Subsequently, the slurry is collected, dried, grinded, sieved, and pressed at 3000 psi into pellets (13 mm diameter). The pellets are sintered at 1100 °C for 3 h and the electrolyte solution (YSZ suspended in ethanol) is spin-coated over one side of the porous NiO-YSZ pellet. The anode-electrolyte assembly is then sintered at 1450 °C for 4 h. The final thickness of the anode and electrolyte layers is ~500 μm and ~15 μm, respectively. A porous YSZ scaffold layer, synthesized as described in Section 2.2.1, is sprayed over the electrolyte side and sintered at 1450 °C. The LNO catalyst is drop coated over the YSZ scaffold, as described in Section 2.2.1, and sintered at 400 °C for 3 h. The final geometric area of the cathode was 0.1 cm^2.

2.3. Electrochemical studies

In all the electrochemical studies, Au mesh (100 LPI, Precision E forming) is used as current collector and Au wires (Alfa Aesar) are used as electrical leads on both electrodes. Au paste (TED Pella) is applied to adhere the electrochemical leads to the electrodes due to its insignificant activity toward oxygen reduction reaction [16]. The cells were attached to the reactor using an Al_2O_3–based paste. Electrochemical Impedance spectroscopy (EIS) studies are performed using a Gamry 300 potentiostat (Gamry Inst. Warminster, PA). All polarization resistances are measured under open circuit conditions (OCV, thermodynamic potential), in a frequency range of 1 MHz–0.01 Hz, with a 10 mV AC perturbation. The symmetric cells are placed in a single chamber reactor under a controlled O_2/N_2 atmosphere (the oxygen partial pressure, P_{O_2}, was varied from 0.04 to 1 atm). EIS experimental data is fitted using the Gamry EIS300 Electrochemical Impedance Spectroscopy Software.

In the case of the electrochemical studies with SOFCs, the NiO/YSZ anode is reduced overnight at 700 °C under a flow of 30% H_2/N_2 (20 ml min^{-1}). Linear sweep voltammetry tests are performed with the SOFC cathode exposed to air and the anode exposed to ultra-high purity hydrogen gas (50 ml min^{-1}). The polarization curves (I–V curves) are obtained from OCV to 0.15 V using a scan rate of 30 mV/s. Electrochemical stability studies are conducted with the SOFC operating in galvanostatic mode at 700 °C with the current density set at 700 mA/cm^2. In these studies the

cathode is left open to air, while the anode is exposed to ultra-high purity hydrogen gas (50 ml min^{-1}).

2.4. Characterization

X-ray diffractometer (XRD, D2 Phaser, Bruker) with Cu Kα radiation (λ = 0.15418 nm) is used to characterize the crystal structure of the electrocatalysts before and after the electrochemical studies. The X-ray diffraction patterns are recorded over 2θ values of 20°–80° with the rate of 0.04°/min.

The morphology and elemental composition of the electrocatalysts are determined using a field-emission scanning electron microscope (FE-SEM, JSM 7600, JEOL Inc., Japan) equipped with an energy dispersive x-ray spectrometer (EDS). SEM and EDS images were obtaining using an accelerating voltage of 15 kV and working distance of 6 mm. Cross-sectional image of the electrode were obtained by blading the pellet in half through the center region of the electrode.

2.4.1. Surface area measurements

The two commonly used approaches for defining the electrode active interfacial area in solid oxide electrochemical cells are: (i) using the geometric area of the electrode [17], and (ii) Newman's method [18], which is mainly used to approximate the triple phase boundary region (TPB, the interface between the electrocatalyst, electrolyte and gas-phase). As we discuss in detail below, in mixed ionic/electronic conducting oxides, such as in the case of LNO, the mechanism that governs ORR involves the entire area of the electrocatalyst and the electrocatalyst/electrolyte interface, and it is not limited to the TPB region. As such, the geometric interfacial area of the electrode (S) – interfacial area between the electrolyte disk and the electrode – is used to approximate the active area of the electrode. This method is only applied to the studies in which the nature of the electrocatalyst is not changed.

In the case when we discuss the effect of the nanostructure of the electrocatalyst (Section 3.4), the cell resistances are normalized by the μmols of O_2 chemisorbed per physical surface area of the electrocatalyst (LNO). This is obtained by combining O_2 chemisorption and N_2 physisorption studies using the Micromeritics ASAP 2020 analyzer. The O_2 chemisorption studies are used to obtain the μmols of O_2 chemisorbed per gram of catalyst, while the N_2 physisorption is used to determine the physical surface area per gram of catalyst. The procedure for O_2 chemisorption studies involves exposing the electrocatalysts to vacuum for 3 h at 300 °C. This is followed by heating the sample to 500 °C in inert atmosphere and exposing it to pure O_2 in a pressure range from 1 to 213.55 mmHg. The amount of O_2 chemisorbed is evaluated by analyzing the plateau region (20–140 mmHg) of the isotherm. In the N_2 physisorption studies, the sample is first degassed under vacuum at 350 °C for 2 h followed by cooling in liquid nitrogen and performing N_2 adsorption–desorption measurements.

All the electrocatalysts are characterized before and after these studies using XRD and SEM to assure that no changes in the structure of the electrocatalysts occurred during these studies.

3. Results and discussion

3.1. Synthesis and characterization of LNO-based electrodes

We have used a reverse microemulsion method to pre-synthesize the desired nanostructures of LNO [11], followed by impregnation of these nanostructures on pre-sintered YSZ electrode scaffolds (See Experimental methods for details). A scanning electron micrograph (SEM) of typical, as-synthesized LNO nanorods is shown in Fig. 1a.

Fig. 1b shows the XRD spectra obtained for the synthesized nanostructured LNO/YSZ electrode before and after the electrochemical studies. These XRD spectra are mainly dominated by
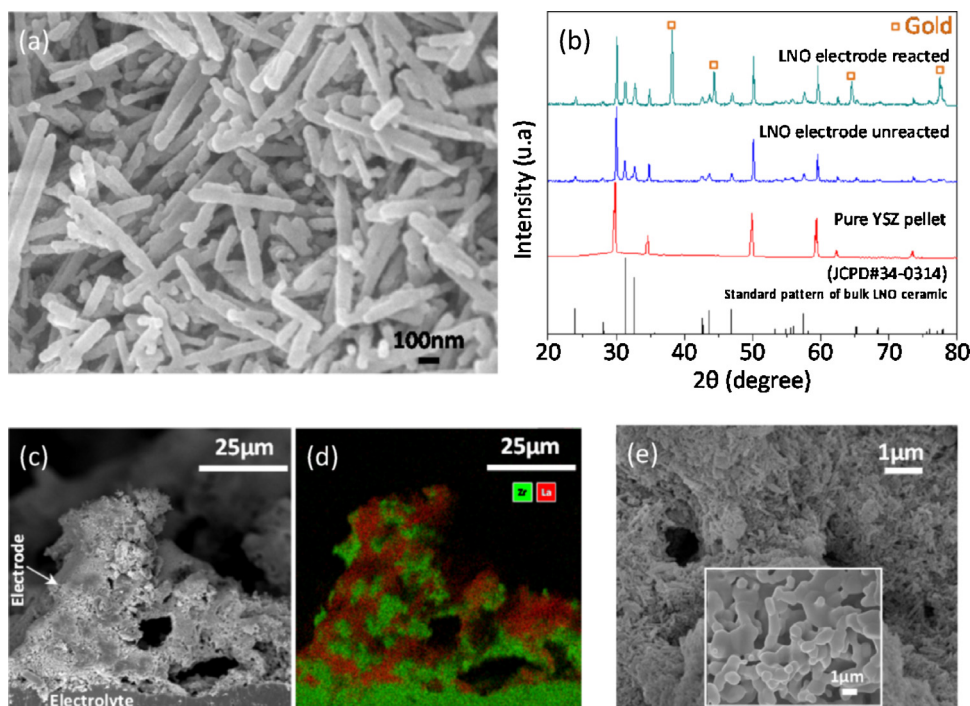

Fig. 1. LNO/YSZ characterization: (a) Scanning electron micrograph (SEM) of LNO nanorods. (b) Standard pattern for bulk LNO ceramics (black) and XRD spectra of pure YSZ pellet/scaffold (red), LNO nanorods supported on YSZ scaffold (LNO/YSZ electrode) (blue) and LNO/YSZ electrode after electrochemical studies (T = 750–550 °C) (green). (c) SEM of LNO/YSZ scaffold electrode (electrode cross-sectional view). (d) Energy dispersive x-ray spectroscopy (EDS) map of the electrode cross-sectional area shown in (c), where the YSZ scaffold is mapped using zirconia (green) and LNO is mapped using lanthanum (red). (e) SEM image showing top view of LNO nanorods coating and pure scaffold (inset). (For interpretation of the references to colour in this figure legend, the reader is referred to the web version of this article.)

peaks associated with LNO, YSZ and gold (current collector) as expected, suggesting that no detectable secondary crystalline phases were formed between LNO and YSZ during the electrochemical studies, and the crystallite structures of LNO and YSZ were preserved after synthesis and EIS studies. Scanning electron microscopic (SEM) (Fig. 1c and e) and energy-dispersive x-ray spectroscopic (EDS) (Fig. 1d) studies show the microstructure of the LNO/YSZ electrode after synthesis. These images demonstrate the uniformity in the distribution of LNO nanorods over the scaffold surface, as well as the preserved nanostructure of LNO rods after synthesis (Fig. 1e). In addition, this approach leads to a fairly large interfacial region between the electrocatalyst and the electrolyte, which should enhance the electrochemical rates.

3.2. Oxygen reduction kinetics using symmetric electrochemical cells

Typical EIS spectra for a symmetric cell containing YSZ scaffolds at the electrode and LNO nanorods (LNO-nanorods/YSZ|YSZ|LNO-nanorods/YSZ) measured at open circuit voltage (OCV), in an oxygen atmosphere ($PO_2 = 1$ atm) and temperatures of 550, 650 and 750 °C are shown in Fig. 2a–c. In these plots $R_{electrolyte}$ describes the ohmic resistance induced by the electrolyte, while $Z_{electrode}$ describes the electrode polarization resistance obtained from the normalization of the raw complex resistance (excludes ohmic resistance) by the electrode geometric interfacial area ($S = 0.1$ cm^2). Fig. 2a–c shows that $Z_{electrode}$ is composed of two main arcs for all temperatures. As the temperature increases, the size of these arcs decreases suggesting that the electrochemical processes that contribute to these resistances are becoming more facile at higher temperatures.

It has been shown that ORR can follow distinct pathways in SOFC cathodes based on the properties of the electrocatalyst and the electrocatalyst/electrolyte interface [25,26]. The predominant pathway in mixed ionic/electronic conducting oxide electrocatalysts has been shown to involve oxygen adsorption, followed by redox oxygen exchange on the electrocatalyst surface

$$(O_{ads} + 2e^- + V_{O(electrocatalyst)}^{..} \Leftrightarrow O_{O(electrocatalyst)}^X,$$
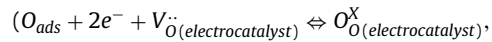
where $V_{O(electrocatalyst)}^{..}$ is an oxygen vacancy in the oxide electrocatalyst and $O_{O(electrocatalyst)}^X$ refers to an oxygen ion in the normal lattice sites of the oxide electrocatalyst, and transport of the oxygen ions through the bulk of the mixed ionic/electronic conducting electrocatalysts to the electrocatalyst/electrolyte interface, where the final step occurs involving the oxygen ion transfer at the electrocatalyst/electrolyte interface ($O_{O electrocatalyst}^X + V_{O electrolyte}^{..} \Leftrightarrow O_{O electrolyte}^X$ [25,26]. Since LNO is a mixed ionic-electronic conducting electrocatalyst that exhibits high ion conductivity [8], a similar pathway is assumed to dominate the ORR kinetics on these materials [2].

In order to identify the steps that limit ORR on LNO nanostructures, an analysis of the polarization resistances that arise from the electrochemical steps that govern ORR on LNO, using an equivalent circuit of the type $LR_e(R_iQ_i)(R_{ii}Q_{ii})$ (Fig. 2d) is conducted. This equivalent circuit model is the best fit to the raw EIS data among the models used to describe ORR on mixed ionic-electronic conducting electrocatalysts. In this model, L accounts for the inductance caused by the electrical connections, R_e represents the ohmic resistance of the YSZ electrolyte, and the circuit elements composed of a resistance in parallel with a constant phase element (R_iQ_i and $R_{ii}Q_{ii}$) represent the two processes that lead to the polarization resistances in the symmetric cells at high frequency (R_iQ_i) and low frequency ($R_{ii}Q_{ii}$) ranges.

The activation barriers for the electrochemical processes governing ORR on electrodes containing LNO nanorod electrocatalyst are obtained from the slopes of the plot of the natural log of the obtained polarization resistances as a function of inverse temperature. This is based on the Arrhenius relationship between the polarization resistance and the activation energy barrier [17]:

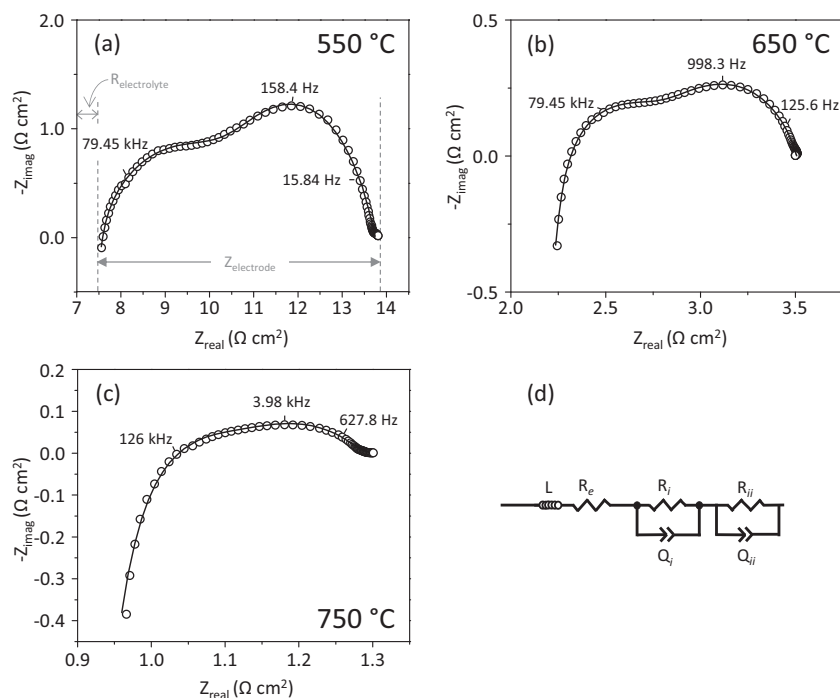$$R_{act} \, T = B \times exp \frac{E_{act}}{RT} \tag{1}$$

Fig. 2. Electrochemical characterization of symmetric cells: Impedance spectra for LNO-nanorods/YSZ|YSZ|LNO-nanorods/YSZ symmetric cells under $P_{O_2} = 1$ atm at an operating temperature of (a) 550 °C, (b) 650 °C (c) 750 °C. The polarization resistance of the electrode ($Z_{electrode}$) is obtained from the normalization of the raw impedance by the electrode area. (d) Equivalent circuit is used to fit of the polarization resistance curves.
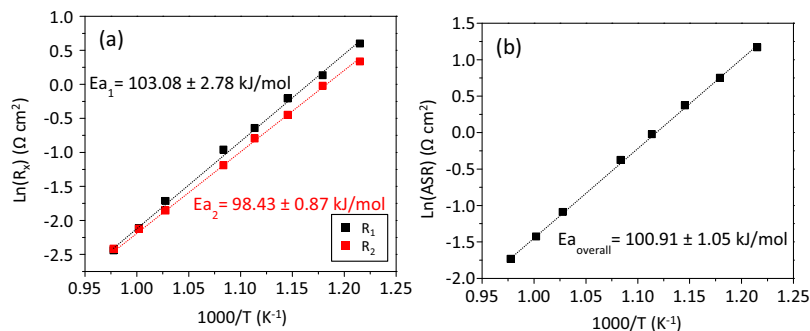
Fig. 3. Kinetics of ORR on symmetric cells containing LNO nanorods: (a) Arrhenius plots of the two main resistances, R_x (x = 1 (■, black) or 2 (■, red)), during ORR on LNO nanorods at P_{O_2} of 1 atm and OCV. (b) Arrhenius plot used to determine the overall activation barrier for ORR on LNO nanorod electrocatalysts. The data is obtained using the average of three independent experimental runs for each case. (For interpretation of the references to colour in this figure legend, the reader is referred to the web version of this article.)

where R_{act} represents the polarization resistance at a given temperature (T), E_{act} is the activation barrier for the process exhibiting the polarization resistance, and B represents the pre-exponential factor (Ω cm^2) related to the electrode active interfacial area.

Initially, we have determined the activation barriers associated with the polarization resistances described by the two main impedance arcs in Fig. 2a–c. Fig. 3a shows the Arrhenius relationships between the polarization resistances (R_1 and R_2) of the two impedance arcs as a function of inverse temperature. R_1 and R_2 are obtained by multiplying the two raw resistances (R_i and R_{ii}) of the electrodes by S/2, in order to normalize by surface area of the electrode (S) and account for the contributions from the two identical electrodes. (See Experimental Methods for details). Based on the slopes of these plots, the activation energies (Ea_1 and Ea_2) associated with the two electrochemical processes described by resistances R_1 and R_2 are calculated to be 103.08 ± 2.78 kJ/mol and 98.43 ± 0.87 kJ/mol, respectively. These activation barriers are very similar in magnitude suggesting that both processes play a significant role in ORR. Fig. 3b shows the overall activation barrier for ORR on LNO nanorods (100.91 ± 1.05 kJ/mol) based on the area specific resistance (ASR), which is calculated as ASR = $Z_{electrode}/2$. This value is significantly lower than the ones reported for traditional perovskite-type electrocatalysts [12–14], suggesting that these materials are promising electrocatalysts for catalyzing ORR at intermediate temperatures.

In order to identify the processes that govern R_1 and R_2, their dependences on the partial pressure of oxygen, and electrocatalyst nanostructure are investigated.

3.3. Dependence of the electrochemical behavior on oxygen partial pressure

In the oxygen partial pressure variation studies, we find that the electrode polarization resistance and P_{O_2} are related as $R \sim a\left(P_{O_2}\right)^{-n}$, similar to literature reports [15,24,27]. The value of n is experimentally found to characterize the nature of the electrochemical step that occurs at the electrode [18]. The following relationships between n and the electrochemical steps in ORR have been reported [18,28]:

When $n=1$, the step involves molecular oxygen adsorption: $\boldsymbol{O_2}$ (g) $\Leftrightarrow \boldsymbol{O_{2,ads}}$
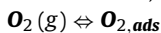
When $n=1/2$, the step involves dissociation of gas-phase oxygen to atomic oxygen: $\boldsymbol{O_{2,ads}} \Leftrightarrow 2\boldsymbol{O_{ads}}$

When $n=1/4$, the step involves charge-transfer/vacancy healing: $\boldsymbol{O}_{ads} + 2\boldsymbol{e^-} + \boldsymbol{V_{\ddot{O}}} \Leftrightarrow \boldsymbol{O_X^0}$

The correlation between the polarization resistances and P_{O_2} are shown in Fig. 4a and b in terms of the linear dependence between the log of the resistances (R_1 and R_2) and the log of P_{O_2}, at high

(700 °C) and low (500 °C) temperatures. The plots show that the polarization resistances decrease as the partial pressure of oxygen increases. From the slopes of the plots in Fig. 4a, n values of 0.08 and 0.125 are obtained. These n values are lower than any of the cases discussed above, making it difficult to relate this resistance to any of the ORR steps mentioned above. On the other hand, the dependence of R_2 on P_{O_2} is higher, with a slope of approximately 0.2 for both temperatures, suggesting that R_2 describes the polarization resistance of a charge-transfer/vacancy healing step ($\boldsymbol{O_{ads}} + 2e^- + \boldsymbol{V_{\ddot{O}}} \Leftrightarrow \boldsymbol{O_{O(LNO)}^X}$).

In order to identify the electrochemical step associated with R_1, the dependence of the capacitance on the partial pressure of O_2 is analyzed. Capacitance values are indicative of the electrode region involved in a particular electrochemical process (i.e., electrocatalyst surface, electrocatalyst bulk, electrocatalyst/electrolyte interface) [15,24,25,29,30]. Capacitance is related to the polarization resistance as:

$$C_x = \frac{(R_x Q_x)^{\frac{1}{k_x}}}{R_x}, \tag{2}$$

where k is a parameter that indicates the similarity of Q (the non-ideal capacitor) to a true capacitor (C), obtained from model fitting. We have calculated the capacitance values associated with both R_1 and R_2 at different oxygen partial pressures and temperatures. We find that the values of C_1 (capacitance associated with R_1) are approximately 10^{-7}–10^{-6} F (Fig. 4c), or 10^{-6}–10^{-5} F/cm^2. These capacitance values fall within the range of the double-layer capacitances [29], and are similar to the interfacial polarization capacitances reported for a Pt/YSZ interface (10^{-6}–10^{-5} F/cm^2) [25]. As such, our results suggest that R_1 is associated with a process at the electrocatalyst/electrolyte interface, such as the oxygen ion transport through this interface, ($\boldsymbol{O_{O(LNO)}^X} + \boldsymbol{V_{\ddot{O}}} \Leftrightarrow \boldsymbol{O_{O(YSZ)}^X}$). This is consistent with literature reports that show that processes with weak oxygen partial pressure dependence and capacitances around 10^{-6} F, are associated with the oxygen ion transport from the electrocatalyst to the electrolyte [15,31]. In the case of R_2, the capacitance values ($\sim 10^{-4}$–10^{-3} F, or 10^{-3}–10^{-2} F/cm^2) are found to be similar to the ones associated with processes involving the adsorption and exchange of oxygen on a Pt electrode ($\sim 10^{-3}$ F/cm^2) [25]. This is consistent with assigning R_2 to overpotential losses associated with the charge-transfer/surface vacancy healing reaction step ($O_{ads} + 2e^- + \boldsymbol{V_{\ddot{O}}} \Leftrightarrow \boldsymbol{O_{O(LNO)}^X}$) [15,24,30,31].

3.4. Dependence of the electrochemical behavior on the electrocatalyst nanostructure

The effect of electrocatalyst nanostructure (well-structured nanorods vs. traditionally used spheres (truncated polyhedrons)) on the electrochemical kinetics associated with ORR on LNO/YSZ
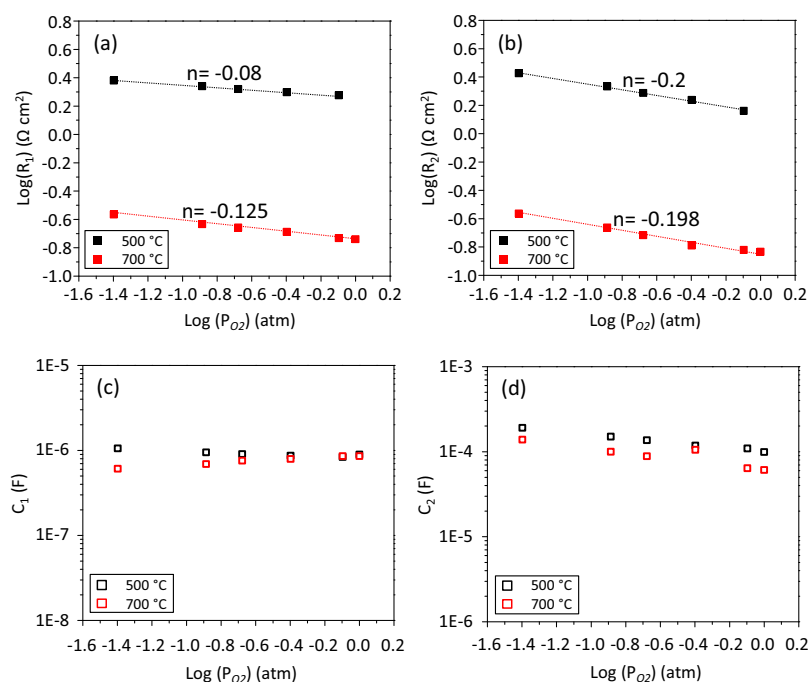
Fig. 4. Dependence of the polarization resistances and capacitances on the oxygen partial pressure: (a) R_1 and (b) R_2 on the oxygen partial pressure at 700 °C (■, red) and 500 °C (■, black). (c) Dependence of capacitance, C_1, on the oxygen partial pressure at 500 °C (□, black) and 700 °C (□, red), and (d) Dependence of C_2 on the oxygen partial pressure at 500 °C and 700 °C. (For interpretation of the references to colour in this figure legend, the reader is referred to the web version of this article.)
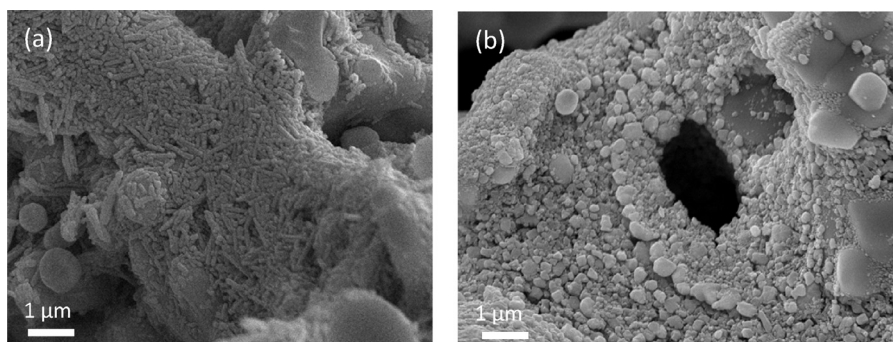

Fig. 5. Scanning electron microscopy of electrodes containing: (a) LNO nanorods and (b) LNO nanospheres.

electrodes is also investigated. In these studies, symmetric cells with porous scaffold electrodes are employed. Fig. 5a and b shows scanning electron micrographs of the scaffold-type electrodes impregnated with LNO nanorods and nanospheres, respectively.

Fig. 6a and b shows the Arrhenius plots (measured from 550 to 700 °C) and the energy barriers associated with the charge transfer/vacancy healing and oxygen ion transport through the electrocatalyst/electrolyte interface steps on porous electrodes containing LNO nanorods and LNO nanospheres. In these plots, the polarization resistances are normalized per μmol of O_2 chemisorbed per surface area of the electrocatalyst (Details are found in the Experimental section). It is clear from these results that the electrodes containing LNO nanospheres exhibit higher activation barriers for both steps ($Ea_{1,nanospheres} = 116.1.087 \pm 1.087$ kJ/mol and $Ea_{2,nanospheres} = 125.84 \pm 6.87$ kJ/mol) than the ones containing LNO nanorods ($Ea_{1,rods} = 103.2.78 \pm 2.78$ kJ/mol and $Ea_{2,rods} = 98.43 \pm 0.87$ kJ/mol). This consistent with our reported density functional theory calculations [11], which showed that (001) NiO terminated surface facets of LNO (that mainly dominate the surface of LNO nanorods) exhibited the highest rates for oxygen exchange as compared to [111], [100] and [001] LaO terminated

LNO surfaces. Our calculations suggested that this was due to the fact that the (001) NiO terminated LNO surface provides the best compromise between the energy associated with surface oxygen vacancy formation and the energy required for dissociative adsorption of oxygen. This is supported by the results obtained here, which show that the symmetric cells containing LNO nanorods exhibit a much lower activation barrier ($Ea_{2,rods} = 98.43 \pm 0.87$ kJ/mol) for the charge transfer/vacancy healing step than symmetric cells containing LNO spheres ($Ea_{2,nanospheres} = 125.84 \pm 6.87$ kJ/mol). We find that the overall ORR activation barrier is lower for cell containing LNO nanorods as compared to the ones with LNO nanospheres. This reinforces the fact that the surface structure of LNO plays a key role in the chemistry-associated with ORR. These findings also demonstrate that the charge transfer/vacancy healing and oxygen ion transport through the electrocatalyst/electrolyte interface steps are key steps at controlling ORR kinetics on nickelate oxides.

3.5. Electrochemical performance of LNO nanostructures in SOFCs

LNO nanostructures are incorporated as cathode electrocatalysts in anode-supported SOFCs. All cells contained identical anodes composed of Ni/YSZ, and thin YSZ electrolytes. The details are
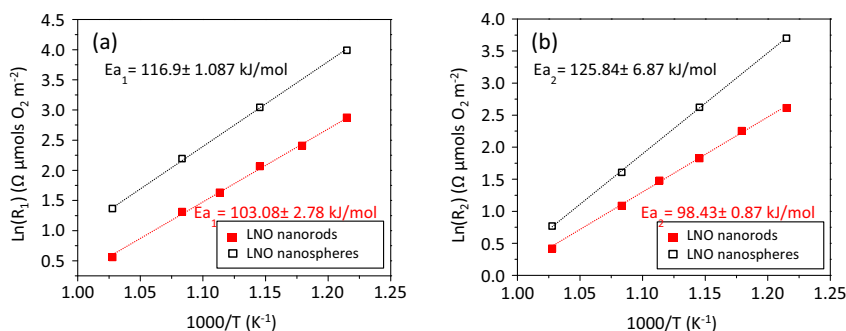
Fig. 6. Kinetics of ORR on LNO electrocatalyst with different nanostructures: Arrhenius plots of (a) R_1 and (b) R_2 for symmetric cells containing LNO nanorods (■, red) *vs.* the ones containing LNO nanospheres (□, black). The data is obtained using the average of three independent experimental runs per each case. (For interpretation of the references to colour in this figure legend, the reader is referred to the web version of this article.)
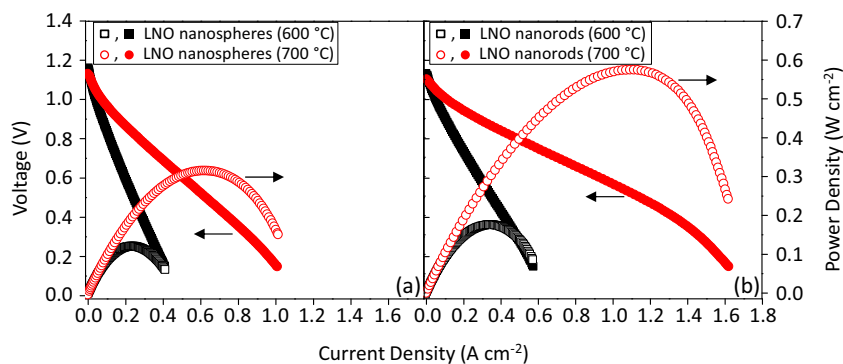

Fig. 7. Electrochemical performance of SOFCs containing LNO electrocatalyst with different nanostructures: (a) LNO nanospheres, and (b) LNO nanorods. Current density (solid markers) and power density (open markers) curves for cells operated at 600 °C (black square) and 700 °C (red circle). (For interpretation of the references to colour in this figure legend, the reader is referred to the web version of this article.)

found in the Experimental section. The cells were tested at different temperatures with the cathode exposed to air, while the anode was exposed to H_2 at a total flow rate of 50 ml min^{-1}. Fig. 7 shows the I–V and power density curves for the SOFCs containing LNO nanospheres (Fig. 7a) and LNO nanorods (Fig. 7b) at the cathode at 600 and 700 °C. Fig. 7 shows that the cells containing LNO nanospheres led to maximum power densities of ∼121 and 321 mW cm^{-2} at 600 and 700 °C, respectively, and current densities of ∼0.41 and 1 A/cm^2 at 600 °C and 700 °C, respectively. The cells containing LNO nanorods achieved much higher power densities of ∼176 and 575 mW cm^{-2} at 600 °C and 700 °C, respectively, and current densities of ∼0.57 and 1.62 A/cm^2 at 600 °C and 700 °C, respectively. Significant improvement in the performance of the SOFCs containing LNO nanorods is observed, especially at 700 °C. At lower temperature (*i.e.* 600 °C) the performance differences between cells containing LNO rods and spheres is not as significant. This is due to the fact that at temperatures below 700 °C, the oxygen conductivity through the YSZ electrolyte starts becoming a challenge [32], and suppresses the impact of the cathode electrocatalyst on the overall performance of the cell. Therefore, the incorporation of the LNO nanorod electrocatalysts in SOFC systems containing high oxygen conducting electrolyte membranes (*i.e.*, cerium-based oxide conductors [33]) should improve the performance of these cells even further at intermediate temperatures [12,13].

Stability of the nanostructure of LNO has also been tested under SOFC operating conditions. Fig. 8a shows the results of the stability test for an anode-supported SOFC with the cathode containing LNO nanorods operated at 700 °C under constant current of 700 mA/cm^2. The cell voltage was monitored over 130 h under these conditions. In this study, the anode was exposed to

50 ml min^{-1} H_2 and the cathode was left open to air. A stable performance was maintained for over 130 h of operation. Fig. 8b and c shows scanning electron micrograph and XRD spectra of the reacted SOFC cathodes containing LNO nanorods, respectively. Fig. 8b and c shows that no changes in the crystal structure (as corroborated by XRD, Fig. 8b) or nanostructure of the catalysts occurred under reaction conditions. These studies suggest that the LNO nanorods, in addition to exhibiting superior performance to LNO spheres, are also very stable under reaction conditions.

4. Conclusions

We have established that there are two main processes that govern ORR on LNO electrocatalysts: charge transfer/surface oxygen vacancy healing at the electrocatalyst/gas interface and oxygen ion transport through the electrocatalyst/electrolyte interface. We find that varying the nanostructure of the LNO (from nanorods to nanospheres (truncated polyhedrons)) significantly affects the activation barriers associated with ORR, with LNO nanorods exhibiting lower overall ORR activation barrier (100.91 ± 1.05 kJ/mol) as compared LNO spheres (120.56 ± 1.76 kJ/mol). We also report that incorporating the LNO nanorods in SOFC cathodes significantly improves the electrochemical cell performance. These findings suggest that (i) enhancing the ORR activity of LNO for operation at intermediate temperatures will require finding ways to lower the activation barriers associated with the charge transfer/surface oxygen vacancy healing and oxygen ion transport through the electrocatalyst/electrolyte interface steps, and (ii) the nanostructure of LNO plays a role in catalyzing these processes and can be used as a tool to improve their activity at intermediate temperatures.
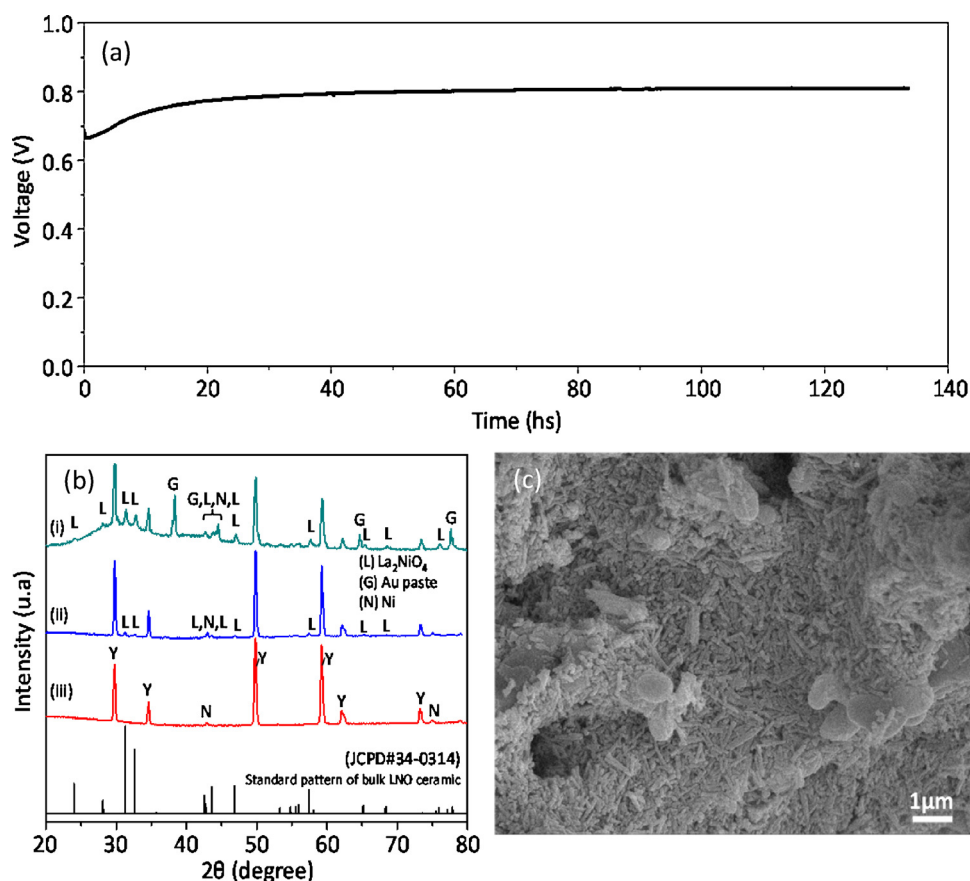
Fig. 8. Stability test of anode-supported SOFC with the cathode containing LNO nanorods: (a) Galvanostatic test (at 700 mA/cm^2) measured over 130 h of SOFC operating at 700 °C with cathode open to air and anode expose to 50 ml min^{-1} H$_2$. (b) XRD spectra of post-reacted cell: (i) SOFC after electrochemical studies, (ii) SOFC before reaction, and (iii) baseline−cell containing NiO/YSZ anode, YSZ electrolyte and cathode YSZ scaffold. Note that gold paste was used for the cell assembly and peaks related to this element can be detected in the post-reacted pellets. (c) Scanning electron micrograph of SOFC cathodes containing LNO nanorods after 130 h of operation.

Acknowledgements

References

[1] C. Xia, W. Rauch, F. Chen, M. Liu, Solid State Ionics 149 (2002) 11–19.
[2] R. Sayers, M. Rieu, P. Lenormand, F. Ansart, J.A. Kilner, S.J. Skinner, Solid State Ionics 192 (2011) 531–534.
[3] F. Chauveau, J. Mougin, F. Mauvy, J.M. Bassat, J.C. Grenier, Int. J. Hydrogen Energ. 36 (2011) 7785–7790.
[4] K.N. Jung, J.H. Jung, W.B. Im, S. Yoon, K.H. Shin, J.W. Lee, Acs Appl. Mater Inter. 5 (2013) 9902–9907.
[5] M.S.D. Read, M.S. Islam, F. King, F.E. Hancock, J. Phys. Chem. B 103 (1999) 1558–1562.
[6] J.C. Grenier, F. Mauvy, C. Lalanne, J.-M. Bassat, F. Chauveau, J. Mougin, J. Dailly, M. Marrony, ECS Trans. 25 (2009) 2537–2546.
[7] H. Zhao, F. Mauvy, C. Lalanne, J.-M. Bassat, S. Fourcade, J.-C. Grenier, Solid State Ionics 179 (2008) 2000–2005.
[8] J.M. Bassat, P. Odier, A. Villesuzanne, C. Marin, M. Pouchard, Solid State Ionics 167 (2004) 341–347.
[9] S.J. Skinner, J.A. Kilner, Ionics 5 (1999) 171–174.
[10] X.F. Ma, J.S.A. Carneiro, X.K. Gu, H. Qin, H.L. Xin, K. Sun, E. Nikolla, ACS Catal. 5 (2015) 4013–4019.
[11] X. Ma, B. Wang, E. Xhafa, K. Sun, E. Nikolla, Chem. Commun. 51 (2015) 137–140.
[12] J.G. Lee, J.H. Park, Y.G. Shul, Nat. Commun. 5 (2014).
[13] Z. Shao, S.M. Haile, Nature 431 (2004) 170–173.
[14] E.P. Murray, T. Tsai, S.A. Barnett, Solid State Ionics 110 (1998) 235–243.
[15] F. Mauvy, C. Lalanne, J.M. Bassat, J.C. Grenier, H. Zhao, L.H. Huo, P. Stevens, J. Electrochem. Soc. 153 (2006) A1547–A1553.
[16] M. Mamak, G.S. Métraux, S. Petrov, N. Coombs, G.A. Ozin, M. Green, J. Am. Chem. Soc. 125 (2003) 5161–5175.
[17] A. Leonide, Y. Apel, E. Ivers-Tiffee, ECS Trans. 19 (2009) 81–109.
[18] E. Siebert, A. Hammouche, M. Kleitz, Electrochim. Acta 40 (1995) 1741–1753.
[19] A.M. Hernández, L. Mogni, A. Caneiro, Int. J. Hydrogen Energy 35 (2010) 6031–6036.
[20] F. Figueiredo, J. Labrincha, J. Frade, F. Marques, Solid State Ionics. 101 (1997) 343–349.
[21] S. Choi, S. Yoo, J.-Y. Shin, G. Kim, J. Electrochem. Soc. 158 (2011) B995–B999.
[22] G. Yang, C. Su, R. Ran, M.O. Tade, Z. Shao, Energ. Fuel 28 (2013) 356–362.
[23] X. Zhang, H. Zhang, X. Liu, J. Power Sources 269 (2014) 412–417.
[24] M.J. Escudero, A. Aguadero, J.A. Alonso, L. Daza, J. Electroanal. Chem. 611 (2007) 107–116.
[25] S.B. Adler, Chem. Rev. 104 (2004) 4791–4844.
[26] A.K. Opitz, M. Kubicek, S. Huber, T. Huber, G. Holzlechner, H. Hutter, J. Fleig, J. Mater. Res. 28 (2013) 2085–2105.
[27] F. Mauvy, J.-M. Bassat, E. Boehm, J.-P. Manaud, P. Dordor, J.-C. Grenier, Solid State Ionics 158 (2003) 17–28.
[28] Y. Takeda, R. Kanno, M. Noda, Y. Tomida, O. Yamamoto, J. Electrochem. Soc. 134 (1987) 2656–2661.
[29] X. Ge, C. Fu, S.H. Chan, Phys. Chem. Chem. Phys. 13 (2011) 15134–15142.
[30] A.P. Khandale, S.S. Bhoga, J. Power Sources 268 (2014) 794–803.
[31] A. Montenegro-Hernández, L. Mogni, A. Caneiro, Int. J. Hydrogen Energy 37 (2012) 18290–18301.
[32] B.C. Steele, A. Heinzel, Nature 414 (2001) 345–352.
[33] E. Ivers-Tiffee, A. Weber, D. Herbstritt, J. Eur. Ceram. Soc. 21 (2001) 1805–1811.